Nanoscale Advances

PAPER

View Article Online
View Journal | View Issue

Cite this: *Nanoscale Adv.*, 2023, **5**, 6238

Open Access Article. Published on 10 October 2023. Downloaded on 10/10/2024 9:31:03 AM.
This article is licensed under a Creative Commons Attribution-NonCommercial 3.0 Unported Licence.

Stable and luminescent cesium copper halide nanocrystals embedded in flexible polymer fibers for fabrication of down-converting WLEDs†

Manav Raj Kar,[a] Kajol Sahoo,[a] Ashutosh Mohapatra[a] and Saikat Bhaumik*[ab]

Received 21st June 2023
Accepted 6th October 2023

DOI: 10.1039/d3na00440f

rsc.li/nanoscale-advances

Recently, $CsPbX_3$ (X = I, Br, Cl) perovskite nanocrystals (NCs) have drawn wide attention owing to their outstanding photophysical and optoelectronic properties. However, the toxicity of such NCs remained a big challenge for further commercialization. Herein, we adopt facile methods for synthesizing green-emissive $Cs_3Cu_2Cl_5$ and blue-emissive $Cs_3Cu_2Br_{2.5}I_{2.5}$ perovskite NCs that exhibit broad emission spectra with large Stokes shifts. These NCs showed photoluminescence quantum yields (PLQY) up to 65% ($Cs_3Cu_2Cl_5$ NCs) and 32% ($Cs_3Cu_2Br_{2.5}I_{2.5}$ NCs) with limited stabilities. To further improve the stability, the NCs were blended with a hydrophobic polymer poly-methylmethacrylate (PMMA) and embedded inside the polymer fiber by an electrospinning process to form composite fibers. The as-prepared $Cs_3Cu_2Cl_5$@PMMA and $Cs_3Cu_2Br_{2.5}I_{2.5}$@PMMA fiber films demonstrated good surface coverage and better thermal stability, and even retained their emission properties when dispersed in water. The emissive fibers were also deposited on flexible polyethylene terephthalate (PET) substrates that displayed high resistance towards bending and twisting with no signs of breakage, damage, or loss of optical properties. Finally, UV-pumped phosphor-converted WLEDs fabricated by using these blue and green-emitting fibers revealed CIE chromaticity coordinates at (0.27, 0.33) with a maximum luminous efficiency of 69 Lm W^{-1} and correlated color temperature (CCT) value of 8703 K. These outcomes can be beneficial for the development of futuristic flexible display technologies.

1. Introduction

In recent years, $CsPbX_3$ (X = I, Br, Cl) perovskite nanocrystals (NCs) have reached greater heights in the fields of different optoelectronic devices due to some of their inimitable properties, like favorable bandgap tunability, high photoluminescence quantum yield (PLQY), narrow emission spectra, high color purity, easy solution processability, *etc.*[1–10] Such unique properties enable them for usage as phosphor materials in the fabrication of highly efficient down-converted WLEDs.[11–16] However, the toxicity of Pb contents towards the environment restricts their commercial applications. Various Pb-free metal cations (*e.g.*, Sn, Ge, Bi, Sb, *etc.*) were explored to substitute the Pb^{2+}-cations in the crystal lattice and then their photophysical properties were studied.[17–28] Sn^{2+} and Ge^{2+} metal cations are the most suitable candidates for the replacement of Pb^{2+}-cations in the perovskite structure because of their nearly similar electronic structure and comparable ionic radii. However, such Sn and Ge-based perovskite materials are chemically unstable and oxidize from +2 to +4 oxidation states.[29,30] Bi and Sb-based perovskite materials construct different crystal structures and have indirect bandgaps, resulting in inferior optical properties.[20,31,32] Double perovskite materials are another possible alternative in which Pb-ions are replaced by a pair of monovalent (*e.g.*, Cu, Ag) and trivalent (*e.g.*, Bi, Sb, In) ions in alternate unit cells to balance the total charge.[24,33–35] However, such double perovskite materials also possess indirect bandgaps and exhibit very low emission intensity.[24,33–35]

Many researchers got interested in 0-D $Cs_3Cu_2X_5$ perovskite materials for their high emission intensity, reasonable stability, low self-absorption, and being earth-abundant materials.[36–39] Here, the Cu-ions are coordinated with halide ions in the crystal to form a tetrahedral crystal structure that triggers Jahn–Teller distortion and results in strong self-trapped exciton (STE) emission.[38] Highly luminescent color tunable $Cs_3Cu_2X_5$ NCs are synthesized either by colloidal hot injection or ligand-assisted re-precipitation (LARP) synthesis methods.[40–42] However, one of the main challenges of these materials is their poor stability under ambient conditions in which the Cu^+-ions oxidize to Cu^{2+}-ions and degrade the perovskite crystal structure.[41] To overcome these challenges, adoption of a suitable synthesis route is required to enhance the stability while maintaining the emission properties of the NCs.

---

[a] *Department of Engineering and Materials Physics, Institute of Chemical Technology-IndianOil Odisha Campus, Bhubaneswar 751013, India*

[b] *Department of Physics, Indian Institute of Technology Guwahati, Assam, 781039, India. E-mail: s.bhaumik@iitg.ac.in*

† Electronic supplementary information (ESI) available. See DOI: **https://doi.org/10.1039/d3na00440f**

© 2023 The Author(s). Published by the Royal Society of Chemistry

Open Access Article. Published on 10 October 2023. Downloaded on 10/10/2024 9:31:03 AM.
This article is licensed under a Creative Commons Attribution-NonCommercial 3.0 Unported Licence.

$CsPbX_3$ NCs degrade rapidly in the presence of heat, moisture, and intense light due to their inherent ionic nature and presence of dynamic capping ligands around them.[43,44] Encapsulation of the perovskite NCs with suitable stable shells (such as metal oxides, metal chalcogenides, and polymers) enhances the NCs' stability.[45–48] Encapsulating $CsPbX_3$ NCs in a high bandgap SiO_2 shell improves the thermal stability of the NCs and also suppresses photo-degradation and anion exchange among the NCs.[49–52] Polymer polyvinyl-pyrrolidone (PVP) and *n*-isopropyl acrylamide (NIPAM) coated around $CsPbX_3$ NCs exhibit better optical properties, higher heat stability, and improved resilience against highly polar solvents.[53,54] $CsPbBr_3$ NCs encapsulated in poly(methyl methacrylate) (PMMA) polymer nano-spheres reveal remarkable water stability for over 80 days.[55] Polystyrene coating around $CsPbBr_3$ NCs resulted in highly monodisperse core–shell NCs with high water, heat, and photostability.[56] Such a core–shell encapsulation strategy has been implemented in Pb-free perovskite NCs, in which $Cs_3Bi_2I_9$, Cs_4SnBr_6, and $Cs_3Cu_2Cl_5$ NCs were coated with SiO_2 shells to achieve higher stability.[40,57,58]

The polymer matrix formation around the NCs is a rather simpler technique that can be used for the protection of the NCs against harsh environments. The perovskite NCs were loaded into a polymer matrix by mixing or blending to form NCs/polymer composites in which the polymer protects the NCs from environmental degradation due to the long molecular chains of such polymers.[59,60] On the other hand, polymeric fibers reveal some unique properties like improved mechanical strength, high flexibility, and high stability owing to their higher surface-to-volume ratio, uniform morphology, and tunable diameter.[61,62] Electrospinning is a facile method for the preparation of composite fibers in which the nanomaterials can be embedded uniformly in polymer fibers while preserving their optical properties.[63,64] Encapsulation of the NCs in electrospun polymer fibers resulted in highly flexible and stable composites that are suitable for futuristic flexible/wearable optoelectronic devices.[65] Metal halide perovskite materials were embedded in polymer fibers that were used for various optoelectronic applications.[66–70] Electrospun polymer fibers can easily overtake the aggregation of NCs by their geometrical confinement, maintaining the phase, optical properties, and quantum confinement effect. Organic–inorganic halide $MAPbX_3$ NCs were enclosed in PAN fibers to achieve highly luminescent and stable films.[66] $CsPbX_3$ NCs were encapsulated in different polymers such as PVP,[67] poly(styrene-butadiene-styrene) (PBS),[68] polystyrene (PS),[69] and poly(methylmethacrylate) (PMMA)[70] fibers that demonstrate strong hydrophobicity and flexibility. The long polymeric chains form compact encapsulation around the perovskite NCs that prevents them from degradation against environmental effects. PMMA is a highly transparent polymer with a high glass transition temperature and widely used as a matrix for perovskite encapsulation.[71,72] The NCs-PMMA composite fibers have high resistance towards heat and moisture owing to the highly hydrophobic nature of PMMA fibres.[63,70] However, to the best of our knowledge, the perovskite encapsulation in polymer fibers is mostly executed with Pb-based perovskites.

Herein, we synthesized Pb-free color-tunable $Cs_3Cu_2Cl_5$ and $Cs_3Cu_2Br_{2.5}I_{2.5}$ perovskite NCs *via* hot injection and LARP synthetic processes, respectively.[40,41] We adopted two different synthesis methodologies to achieve the best quality of respective NCs with high emission intensity and stability. The NCs are highly crystalline, have uniform size distribution, and fairly good optical properties with limited stabilities. To further increase the stability, we embedded these NCs in PMMA polymer fibers *via* an electrospinning process and studied their physical and optical properties. We examined the heat and water stabilities of these bare NCs and NCs@polymer fiber based films. We also studied the flexibility and durability of these fibers against mechanical stress like bending and twisting for several cycles after coating them on flexible PET substrates. Finally, the composite fibers were tested as phosphors for down-converted WLEDs.

2. Experimental section

2.1. Materials

Cesium carbonate (Cs_2CO_3, 99.9%), 1-octadecene (ODE, 99.9%), chloroform ($CHCl_3$, 99.9%), copper chloride (CuCl, 99.9%), copper bromide (CuBr, 99.9%), copper iodide (CuI, 99.9%), cesium bromide (CsBr, 99.9% trace metals basis), dimethyl sulfoxide (DMSO, 99.9%), oleic acid (OAc, 90%), oleylamine (OAm, 70%), toluene (anhydrous, 99.8%), and poly(methylmethacrylate) (PMMA, MW-350 000, 99.9%) were purchased from Sigma-Aldrich company. All the chemicals were used without further purification.

2.2. Synthesis of $Cs_3Cu_2Cl_5$ NCs

The $Cs_3Cu_2Cl_5$ NCs were synthesized by following the reported hot injection synthesis route.[40] In detail, 305 mg Cs_2CO_3, 15 mL ODE, and 1 mL OAc were loaded into a 100 mL three-neck round bottom flask (flask-1) to prepare the Cs-precursor. 39.6 mg CuCl and 10 mL ODE were loaded into another 100 mL three-neck round bottom flask (flask-2). The two flasks were first degassed for 15 min. Then both flasks were heated to 120 °C, followed by quick addition of 0.5 mL OAc and 0.5 mL OAm into flask-2 at 120 °C under nitrogen flow. After CuCl powders were completely dissolved, the reaction temperature was maintained at 120 °C for 10 min. Finally, 3 mL Cs-precursor was quickly injected into flask-2 and the mixture was cooled in an ice-water bath to room temperature in 5 s. The as-prepared crude NC solution was centrifuged at 6000 rpm for 15 min and the supernatant was discarded. The final precipitate was dispersed in $CHCl_3$. The schematic diagram of the synthesis process is shown in Fig. S1 (see ESI†).

2.3. Synthesis of $Cs_3Cu_2Br_{2.5}I_{2.5}$ NCs

The $Cs_3Cu_2Br_{2.5}I_{2.5}$ NCs were synthesized by following the reported LARP synthesis route.[41] In detail, 0.06 mmol CsBr, 0.015 mmol CuBr, and 0.015 mmol CuI were dissolved in 750 μL DMSO to form the final precursor solution. 200 μL precursor solution was injected into 5 mL toluene along with 250 μL of OAc under vigorous stirring conditions. Then the solution was

Open Access Article. Published on 10 October 2023. Downloaded on 10/10/2024 9:31:03 AM. This article is licensed under a Creative Commons Attribution-NonCommercial 3.0 Unported Licence.

centrifuged at 6000 rpm for 15 min followed by dispersion of the final precipitate in $CHCl_3$. The schematic diagram of the synthesis process is shown in Fig. S1 (see ESI†).

2.4. Electrospinning of the perovskite NCs@PMMA fiber film

The NCs@PMMA fiber film was prepared by mixing either $Cs_3Cu_2Cl_5$ (5 mg mL^{-1}) or $Cs_3Cu_2Br_{2.5}I_{2.5}$ NCs (10 mg mL^{-1}) in PMMA/$CHCl_3$ solution (20 wt% or 298 mg mL^{-1}) which was then loaded in a 10 mL syringe. The weight ratio for $Cs_3Cu_2Cl_5$: PMMA was maintained at ~1 : 60, and that for $Cs_3Cu_2Br_{2.5}I_{2.5}$: PMMA was ~1 : 30. The syringes were positioned horizontally on an electrospinning workstation consisting of a high-voltage power supply, a digitally controlled syringe pump, and a rotating metal drum collector. The high voltage electrode was clamped to the needle tip and the ground was connected to the rotating drum (collector) covered with aluminium foil. The fibers were collected on glass and PET substrates fixed over the aluminium foil. Different potential voltages (in kV) were applied between the syringe and collector set at a distance of 10 cm. The solution flow rate was fixed at 1 mL h^{-1} and the rotation speed of the drum was set to 150 rpm min^{-1} for the collection of fibers. The entire experiment was carried out at 25–30 °C under 40–50% relative humidity. The schematic diagram of fiber preparation is shown in Fig. S1 (see ESI†).

3. Results and discussion

The absorption and PL emission spectra of $Cs_3Cu_2Cl_5$ NCs were recorded in the solution phase and the corresponding plots are shown in Fig. 1a. From the absorption spectrum, it can be observed that the absorbance of $Cs_3Cu_2Cl_5$ NCs increases significantly from around 450 nm and continues to increase with a decrease in wavelength values. The bandgap of the NCs is calculated to be around 2.6 eV (~477 nm) (see Fig. 1b).[73] The PL spectrum of the $Cs_3Cu_2Cl_5$ NCs reveals a PL peak position at 527 nm with a broad full width at half maximum (FWHM) of ~105 nm. The photographic image of the $Cs_3Cu_2Cl_5$ NC solution under a 280 nm UV lamp is shown in the inset of Fig. 1a, which reveals green color emission from the NCs. The absorption spectrum of $Cs_3Cu_2Br_{2.5}I_{2.5}$ NCs exhibits an absorption maximum situated at 302 nm, as presented in Fig. 1c. The PL spectrum of these NCs has an emission maximum at 465 nm in the blue region with a FWHM of ~91 nm (see Fig. 1c). The inset of Fig. 1c shows a photograph of $Cs_3Cu_2Br_{2.5}I_{2.5}$ NCs showing blue emission under a 280 nm UV lamp. The Tauc plot of $Cs_3Cu_2Br_{2.5}I_{2.5}$ NCs is presented in Fig. 1d that reveals a bandgap of around 3.6 eV (~344 nm). The PLQY for $Cs_3Cu_2Cl_5$ NCs was calculated to be around 65%, and that of $Cs_3Cu_2Br_{2.5}I_{2.5}$ NCs was 32%. The broad PL emission and large stokes shift are some of the unique optical properties that can be seen in $Cs_3Cu_2X_5$ NCs, originating from STE emissions from the recombination of excitons.[74–77] STE emission is generated by lattice distortion (Jahn–Teller distortion) induced by the strong electron-phonon coupling upon excitation of photons and responsible for such a broad emission spectrum with large Stokes shifts.[78] A broad emission spectrum is beneficial for WLED applications as it can cover the entire visible spectrum.

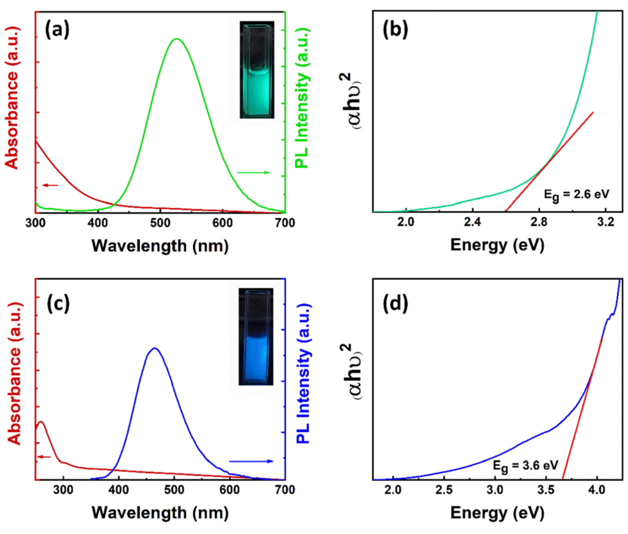

Fig. 1 (a) Absorption and PL spectra of $Cs_3Cu_2Cl_5$ NCs. Inset: photographic image of the $Cs_3Cu_2Cl_5$ NC solution under a UV lamp. (b) Tauc plot of $Cs_3Cu_2Cl_5$ NCs. (c) Absorption and PL spectra of $Cs_3Cu_2Br_{2.5}I_{2.5}$ NCs. Inset: photographic image of the $Cs_3Cu_2Br_{2.5}I_{2.5}$ NC solution under a UV lamp. (d) Tauc plot of $Cs_3Cu_2Br_{2.5}I_{2.5}$ NCs.

Further, to illustrate the crystal structures of $Cs_3Cu_2Cl_5$ and $Cs_3Cu_2Br_{2.5}I_{2.5}$ NCs, we conducted X-ray diffraction (XRD) studies in thin-film form. The stacked XRD patterns of the NCs are shown in Fig. 2a. The diffraction spectrum for $Cs_3Cu_2Cl_5$ NCs matches quite well with the orthorhombic crystal structure of the $Cs_3Cu_2Cl_5$ phase (PDF#04-019-9644) in which Cu^+-ions are coordinated with Cl^--ions in a tetrahedral fashion (see inset of Fig. 2a).[41] The unit cell parameters for $Cs_3Cu_2Cl_5$ crystal phases are calculated to be $a = 15.4510$ Å, $b = 8.75935$ Å, and $c = 8.68517$ Å. The diffraction spectrum of $Cs_3Cu_2Br_{2.5}I_{2.5}$ NCs is somewhat similar to that of $Cs_3Cu_2Cl_5$ NCs, indicating the possibility of a similar orthorhombic phase.[41] However, the diffraction peaks situated at 20.01°, 28.71°, 35.17°, and 41.29° are slightly shifted towards higher angles which could be ascribed to the larger anionic radius of Br^- and I^--ions compared to that of Cl^--ions. To determine the shape and size of the NCs, transmission electron microscopy (TEM) measurement was conducted. The TEM images of $Cs_3Cu_2Cl_5$ NCs and $Cs_3Cu_2Br_{2.5}I_{2.5}$ NCs are shown in Fig. 2b and d, respectively. The TEM images of both NCs reveal a spherical shape of the NCs with uniform and monodisperse size distribution. The average diameters of the $Cs_3Cu_2Cl_5$ NCs and $Cs_3Cu_2Br_{2.5}I_{2.5}$ NCs are 4.66 ± 1 (see Fig. 2c) and 4.88 ± 1 nm (see Fig. 2e), respectively.

Fourier-transform infrared (FTIR) spectra of both the NCs were recorded to identify the presence of passivating agents/ligands around the NC surface and the corresponding spectra are shown in Fig. 3a. The FTIR spectrum of $Cs_3Cu_2Cl_5$ NCs reveals strong absorption peaks situated at 2924 cm^{-1}, 2853 cm^{-1}, and 1273 cm^{-1} that suggest asymmetric $-CH_2$ stretching, symmetric $-CH_2$ stretching, and C–O stretching, respectively, originating from passivating OAc ligands.[79] The vibration peaks at 1651 cm^{-1} and 3336 cm^{-1} signify N–H

© 2023 The Author(s). Published by the Royal Society of Chemistry

Open Access Article. Published on 10 October 2023. Downloaded on 10/10/2024 9:31:03 AM.
This article is licensed under a Creative Commons Attribution-NonCommercial 3.0 Unported Licence.

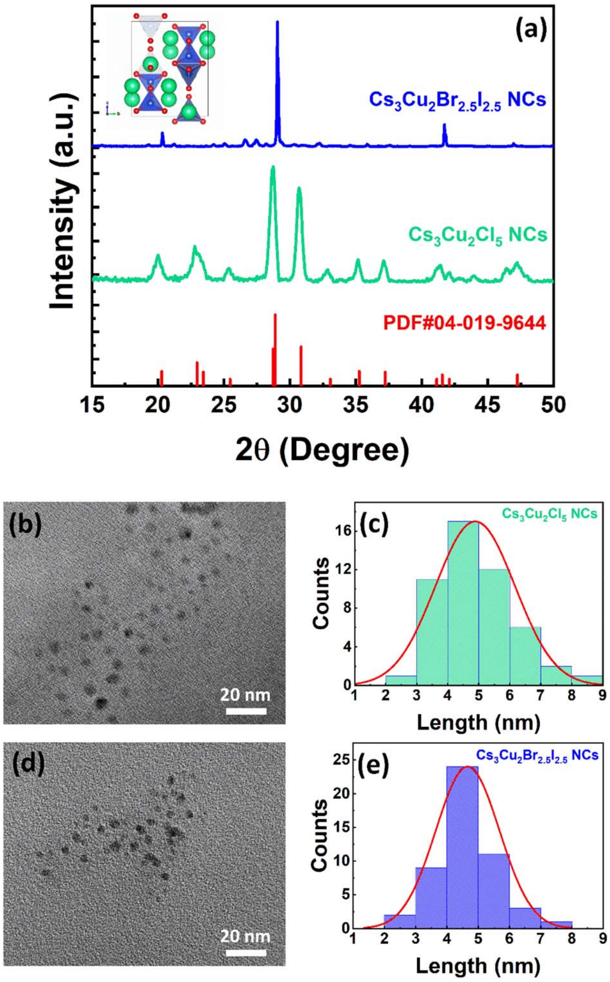

Fig. 2 (a) Stacked XRD diffraction patterns of $Cs_3Cu_2Cl_5$ NCs (green line) and $Cs_3Cu_2Br_{2.5}I_{2.5}$ NCs (blue line) in film form. Bottom vertical lines of the figure represent the standard XRD diffraction pattern of orthorhombic $Cs_3Cu_2Cl_5$ crystal structure (PDF#04-019-9644). Inset: Schematic diagram of $Cs_3Cu_2Cl_5$ crystal, where green, blue, and red balls are Cs, Cu and Cl-atoms, respectively. (b) TEM image and (c) particle size distribution of $Cs_3Cu_2Cl_5$ NCs. (d) TEM image and (e) particle size distribution of $Cs_3Cu_2Br_{2.5}I_{2.5}$ NCs.

bending vibrations and N–H stretching vibrations for the OAm ligands.[80] These results indicate that the OAc and OAm ligands effectively passivate the $Cs_3Cu_2Cl_5$ NCs that were synthesized *via* the hot injection method. For $Cs_3Cu_2Br_{2.5}I_{2.5}$ NCs, the absorption peaks in the FTIR spectrum located at 2920 cm^{-1}, 2851 cm^{-1}, and 1459 cm^{-1} correspond to asymmetric $-CH_2$ stretching, symmetric $-CH_2$ stretching, and –OH stretching that belong to the OAc ligand.[79] Additionally, the absorption peak situated at 1713 cm^{-1} signifies the asymmetric $-C{=}O$ bonding vibrations of OAc ligands. The broad shoulder in the region between 3398 cm^{-1} could be assigned to the dimers of OAc[81] since the $Cs_3Cu_2Br_{2.5}I_{2.5}$ NCs were synthesized *via* the LARP synthesis method and the OAc ligand was only used during the NC synthesis. So, the corresponding FTIR spectrum confirms the presence of only OAc ligands around the NCs.

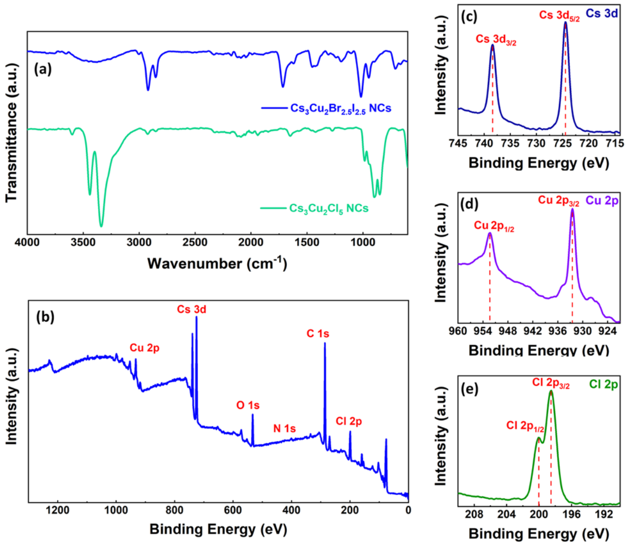

Fig. 3 (a) Stacked FTIR spectra of $Cs_3Cu_2Cl_5$ and $Cs_3Cu_2Br_{2.5}I_{2.5}$ NCs as shown in a legend. (b) Core XPS spectrum of $Cs_3Cu_2Cl_5$ NCs. High resolution XPS spectra of (c) Cs 3d, (d) Cu 2p, and (e) Cl 2p chemical states.

The core X-ray photoelectron spectrum (XPS) for $Cs_3Cu_2Cl_5$ NCs is presented in Fig. 3b. It was recorded to confirm the presence of Cs, Cu, and Cl-ions in the lattice. The high-resolution XPS (HRXPS) spectrum of Cs 3d reveals two binding energy maxima centered at 724.4 eV and 738.3 eV corresponding to Cs $3d_{5/2}$ and $3d_{3/2}$ chemical states (see Fig. 3c), respectively.[73,78] The two binding energy peaks located at 932.4 eV and 952.3 eV in the HRXPS spectrum of Cu 2p, signify Cu $2p_{3/2}$ and $2p_{1/2}$ chemical states as shown in Fig. 3d, indicating the existence of monovalent Cu^+-ions.[73,78,82,83] The HRXPS spectrum of Cl 2p (see Fig. 3e) reveals two binding energy peaks at 198.5 eV and 200.1 eV that can be attributed to Cl $2p_{3/2}$ and $2p_{1/2}$ chemical states.[82] The XPS signal maxima for C 1s, N 1s, and O 1s chemical states are shown in Fig. S2 (ESI†). The peaks of C 1s, N 1s, and O 1s chemical states appear as a contribution from the attached ligands to the NC surface. The XPS signal peak for the C 1s chemical state is obtained at 285 eV, which depicts the aliphatic carbon chain.[84] It can be noticed that the XPS signal for the N 1s chemical state has a peak at 400.1 eV, and an additional satellite peak is obtained at 402.3 eV that represents the nitrogen present in the amine groups of OAm ligands. On the other hand, the binding energy peak at 532.4 eV from the O 1s chemical state can be assigned to two non-equivalent oxygen atoms originating from the carboxylic acids of OAc ligands.[85]

In order to enhance the stability of the NCs, we embedded the NCs in PMMA fibers that were grown *via* the electrospinning process. We optimized the electrospinning process to achieve high-quality fibers with higher film surface coverage. The most crucial factors that influence the fiber formation are the viscosity and surface tension of the polymer solution. The concentration of NCs in the solution also impacts the luminescence of the film. Initially, we optimized the PMMA concentration to 20 wt% or 298 mg mL^{-1} in chloroform. We observed that if the concentration of the polymer is lower (*i.e.*, 15 wt%) it creates extremely thin fibers with excessive bead

Open Access Article. Published on 10 October 2023. Downloaded on 10/10/2024 9:31:03 AM.
This article is licensed under a Creative Commons Attribution-NonCommercial 3.0 Unported Licence.

formation, as visible from the fluorescence microscopy and FESEM images shown in Fig. S3a and b, respectively (see ESI†). On the other hand, the solution can't reach the substrate at higher concentrations (*i.e.*, 25 wt%) due to the high viscosity.

Then we optimized the operating voltage in the range of 15–20 kV (~18 kV) which shows nearly uniform film morphology as depicted in Fig. S3c (see ESI†). Voltages lower than this range (*i.e.*, 10 kV) resulted in the formation of very thin and uneven fibers with inadequate surface coverage as seen in Fig. S3d (see ESI†). Conversely, higher voltages (*i.e.*, 25 kV) halted fiber formation due to the instability of the vibrating Taylor cone and increased branching of the cone. Finally we focused on optimizing the concentrations of the NC solution in which 5 mg mL^{-1} for $Cs_3Cu_2Cl_5$ and 10 mg mL^{-1} for $Cs_3Cu_2Br_{2.5}I_{2.5}$ NCs were found to be optimal. Concentrations lower than these led to low emission intensity from the film, while excessive concentrations led to the formation of beads.

In order to determine the fiber morphology, diameter, and shape, high-resolution (HR) FESEM images of the $Cs_3Cu_2Cl_5$@PMMA and $Cs_3Cu_2Br_{2.5}I_{2.5}$@PMMA fibers were recorded and compared with those of the respective NC films. The HR-FESEM images of $Cs_3Cu_2Cl_5$ (see Fig. 4a) and $Cs_3Cu_2Br_{2.5}I_{2.5}$ NCs (see Fig. 4e) reveal fusion of smaller NCs with one another to form bigger particles (appear as dark grey chunks). The degree of agglomeration of $Cs_3Cu_2Br_{2.5}I_{2.5}$ NCs is found to be somewhat higher than that of $Cs_3Cu_2Cl_5$ NCs, showing pinholes (black regions) on the surface. On the other hand, HR-FESEM images of $Cs_3Cu_2Cl_5$@PMMA (see Fig. 4b) and $Cs_3Cu_2Br_{2.5}I_{2.5}$@PMMA (see Fig. 4f) fibers exhibit the nanowire morphology, having diameters ranging from 6 to 12 µm. The zoomed images of $Cs_3Cu_2Cl_5$@PMMA and $Cs_3Cu_2Br_{2.5}I_{2.5}$@PMMA fibers are shown in Fig. 4c and g, respectively. Both the fiber surfaces reveal porous surface morphology, and the pores are oval-shaped.[86] The average fiber diameter for the $Cs_3Cu_2Cl_5$@PMMA fiber is observed to be around 10 µm and that of $Cs_3Cu_2Br_{2.5}I_{2.5}$@PMMA fibers is about 8 µm. The elemental color mapping of the $Cs_3Cu_2Cl_5$@PMMA fibers and $Cs_3Cu_2Br_{2.5}I_{2.5}$@PMMA fibers is presented in Fig. 4d and h, respectively. The color mapping data clearly show the presence of higher counts of Cs, Cu, and Cl atoms for $Cs_3Cu_2Cl_5$@PMMA fibers and Cs, Cu, Br, and I elements for $Cs_3Cu_2Br_{2.5}I_{2.5}$@PMMA fibers in the regions where fibers are noticed on top of the substrate. The elemental analysis of the composite fibers was analyzed by the energy-dispersive X-ray spectroscopy (EDS) experiment, and the corresponding data are presented in Fig. S4 (see ESI†). The Cs : Cu : Cl atomic ratios obtained from the EDS of $Cs_3Cu_2Cl_5$ NCs are close to 3 : 2 : 5, which matches well with the composition of the NCs. The elemental ratio of Cs : Cu : Br : I atoms in $Cs_3Cu_2Br_{2.5}I_{2.5}$ NCs is found to be close to 3 : 2 : 2.5 : 2.5, confirming the formation of the corresponding NC phase. In the case of $Cs_3Cu_2Cl_5$@PMMA and $Cs_3Cu_2Br_{2.5}I_{2.5}$@PMMA fibers, elemental ratios are also found to be similar to the corresponding NCs that confirms the encapsulation of the NCs inside the PMMA fibers.

To distinguish the morphology and coverage of the fibers on glass substrates, fluorescence microscopy and low-resolution field emission scanning electron microscopy (LR-FESEM) of $Cs_3Cu_2Cl_5$@PMMA and $Cs_3Cu_2Br_{2.5}I_{2.5}$@PMMA fibers were carried out and the corresponding results are compared with the LR-FESEM images of bare $Cs_3Cu_2Cl_5$ and $Cs_3Cu_2Br_{2.5}I_{2.5}$ NCs. The fluorescence microscopy images of the NCs and fibers are shown in Fig. 5 and the insets represent the respective LR-FESEM images. From the fluorescence and LR-FESEM images, it can be observed that the surface coverage of the fibers on the substrate is better than that of NC thin-films which results from the agglomeration of isolated NCs on certain regions of the substrate forming large chunks as seen from Fig. 5a and c. On the contrary, the $Cs_3Cu_2Cl_5$@PMMA and $Cs_3Cu_2Br_{2.5}I_{2.5}$@PMMA fibers are uniformly distributed over the surface of the substrate (see Fig. 5b and d). The reason for such agglomeration of NCs might be due to the dynamic nature of ligands that eventually detach from the NC surface when drop-cast on the substrate.[43] As a result, NCs attach with each other, forming bigger particles. In the case of the fibers, the NCs are

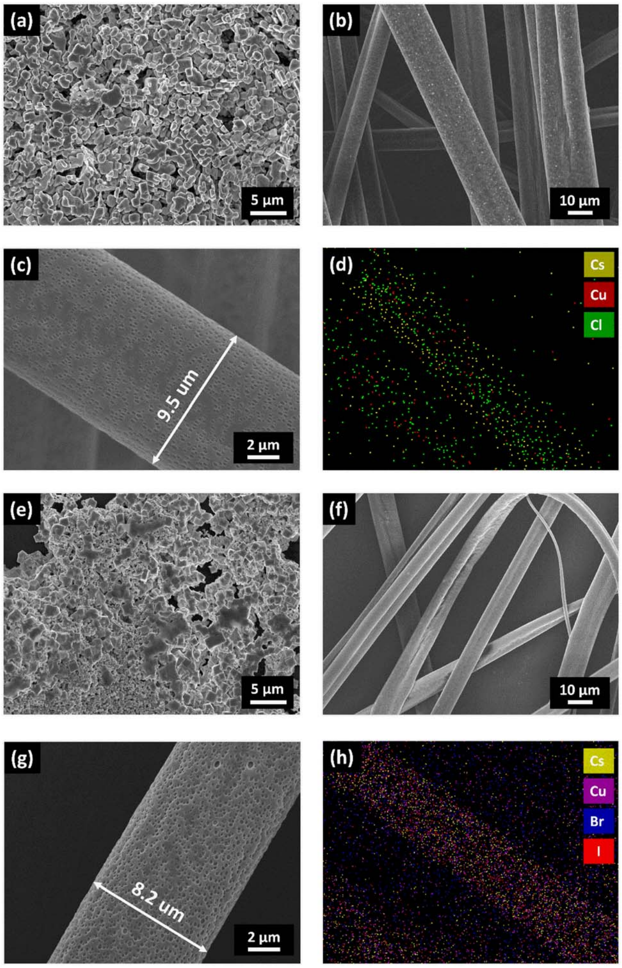

Fig. 4 HR-FESEM images of (a) $Cs_3Cu_2Cl_5$ NCs and (b) $Cs_3Cu_2Cl_5$@PMMA fibers coated on glass substrates. (c) Zoomed image of a single $Cs_3Cu_2Cl_5$@PMMA fiber strand. (d) Elemental color mapping of $Cs_3Cu_2Cl_5$@PMMA fibers. HR-FESEM images of (e) $Cs_3Cu_2Br_{2.5}I_{2.5}$ NCs and (f) $Cs_3Cu_2Br_{2.5}I_{2.5}$@PMMA fibers. (g) Zoomed image of a single $Cs_3Cu_2Br_{2.5}I_{2.5}$@PMMA fiber strand. (h) Elemental color mapping of $Cs_3Cu_2Br_{2.5}I_{2.5}$@PMMA fibers.

Open Access Article. Published on 10 October 2023. Downloaded on 10/10/2024 9:31:03 AM.
This article is licensed under a Creative Commons Attribution-NonCommercial 3.0 Unported Licence.

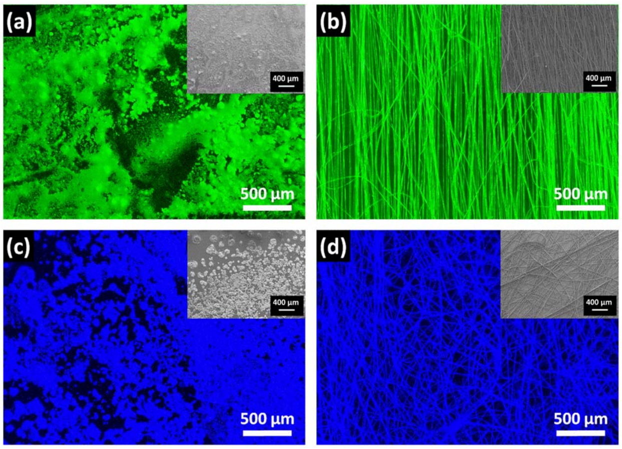

Fig. 5 Fluorescence microscopy images of (a) $Cs_3Cu_2Cl_5$ NCs, (b) $Cs_3Cu_2Cl_5$@PMMA fibers, (c) $Cs_3Cu_2Br_{2.5}I_{2.5}$ NCs, and (d) $Cs_3Cu_2Br_{2.5}I_{2.5}$@PMMA fibers coated on different glass substrates. Insets: LR-FESEM images of (a) $Cs_3Cu_2Cl_5$ NCs, (b) $Cs_3Cu_2Cl_5$@PMMA fiber, (c) $Cs_3Cu_2Br_{2.5}I_{2.5}$ NCs, and (d) $Cs_3Cu_2Br_{2.5}I_{2.5}$@PMMA fiber films.

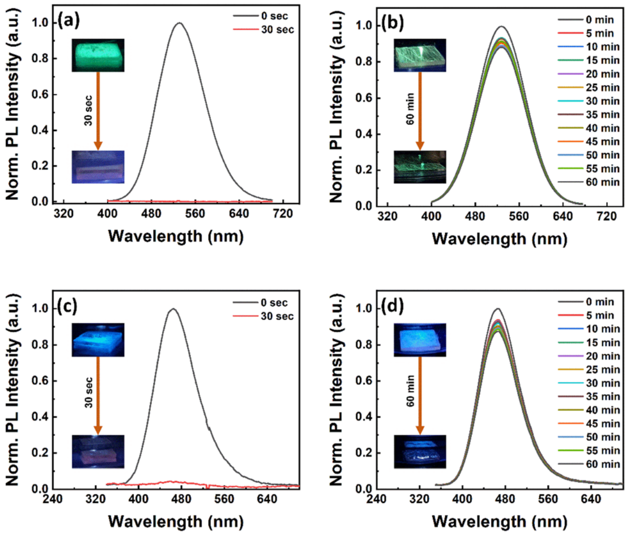

Fig. 6 Water stability test: change in PL intensity of (a) $Cs_3Cu_2Cl_5$ NCs, (b) $Cs_3Cu_2Cl_5$@PMMA fiber, (c) $Cs_3Cu_2Br_{2.5}I_{2.5}$ NCs, and (d) $Cs_3Cu_2Br_{2.5}I_{2.5}$@PMMA fiber films with respect to dipping time in DI water, as shown in legends. Insets: photographic images of respective films before and after dipping in DI water.

monodisperse and are embedded in the fiber matrix which ensures uniform coating over the glass substrates.

The superior stability of the NCs against harsh external environments is necessary for practical applications. In order to determine the degree of hydrophobicity or moisture diffusion, the contact angles of the NCs@PMMA fibers in film form and bare NC films were measured. The photographic images of contact angles of water on NCs films and fibers are shown in Fig. S5a–d (see ESI†). The contact angle is a measurement of the degree of wettability of a liquid on a solid surface which describes the nature of the interaction between them. The contact angles for $Cs_3Cu_2Cl_5$ and $Cs_3Cu_2Br_{2.5}I_{2.5}$ NC films were calculated to be 79.6° and 58.6°, respectively. The acute angle indicates the hydrophilic nature of the films that allow the water droplet to wet the surface. Comparatively, the contact angles of the $Cs_3Cu_2Cl_5$@PMMA and $Cs_3Cu_2Br_{2.5}I_{2.5}$@PMMA fibers were found to be 126.2° and 127.8°, respectively. The higher/obtuse contact angle values for fibers indicate hydrophobic interaction between the surface and water droplet. This hydrophobic nature of the fiber surface protects the embedded NCs inside from moisture invasion, thus protecting them from degradation.

The high contact angle results encouraged us to test the stability of our fibers in water. We tested the water stability of the NC films and fibers that were coated on glass substrates. In this regard, NCs and fiber-coated glass substrates were immersed in a Petri-dish containing DI water and then PL spectra of the samples were recorded at regular time intervals. The PL spectra of $Cs_3Cu_2Cl_5$ NCs, $Cs_3Cu_2Cl_5$@PMMA fiber, $Cs_3Cu_2Br_{2.5}I_{2.5}$ NCs, and $Cs_3Cu_2Br_{2.5}I_{2.5}$@PMMA fiber films are presented in Fig. 6a–d. It can be observed that the bare $Cs_3Cu_2Cl_5$ and $Cs_3Cu_2Br_{2.5}I_{2.5}$ NC films degrade instantly upon contact with DI water and cause a sharp decrease in PL intensity. After mere 30 s, the recorded PL intensity of these NCs almost quenches which describes the extremely low stability of the bare NCs in water. Such instant emission quenching relates to the oxidation of the perovskite phase and decomposition into precursor salts.[40] On the other hand, the PL intensity of the $Cs_3Cu_2Cl_5$@PMMA fiber film retains 93% and 88% of its initial PL intensity after 30 and 60 min immersion in DI water, respectively. Similarly, the PL intensity of $Cs_3Cu_2Br_{2.5}I_{2.5}$@PMMA fiber films shows 91% and 87% of their initial PL intensity after 30 and 60 min, respectively. Insets of Fig. 6a–d display photographic images of the corresponding films before and after immersion in DI water. These observations predict that the NCs are not situated outside the fiber but are embedded inside the fiber matrix. The outer layer of the PMMA fiber serves as a hydrophobic surface that repels the water molecules from entering inside the matrix and protects the degradation of the NCs.

Heat stability of the NCs is another essential factor for the fabrication of efficient LEDs since long working hours may heat up the device and cause degradation. The heat stability of the NCs and respective fibers was tested at different temperatures in film form by placing them on a hot plate. The temperature of the hot plate was increased at a step of 10 °C starting from 30 °C and the corresponding PL spectra of the films were recorded as shown in Fig. 7. The PL intensity of the $Cs_3Cu_2Cl_5$ NC films decreases slowly up to 70 °C, while the rate of PL quenching is much faster above 70 °C, as can be seen from Fig. 7a. The maximum temperature that the NC film can sustain is around 170 °C. For the $Cs_3Cu_2Br_{2.5}I_{2.5}$ NC film, the temperature resistance is found to be lower compared to the $Cs_3Cu_2Cl_5$ NC film, which signifies the lower phase stability of mixed halide perovskites.[87] The PL intensity of the $Cs_3Cu_2Br_{2.5}I_{2.5}$ NC film decreases much faster and the highest temperature it could survive is around 80 °C, as shown in Fig. 7c. Conversely, the fibers had higher heat resistivity at a specific temperature

Open Access Article. Published on 10 October 2023. Downloaded on 10/10/2024 9:31:03 AM.
This article is licensed under a Creative Commons Attribution-NonCommercial 3.0 Unported Licence.

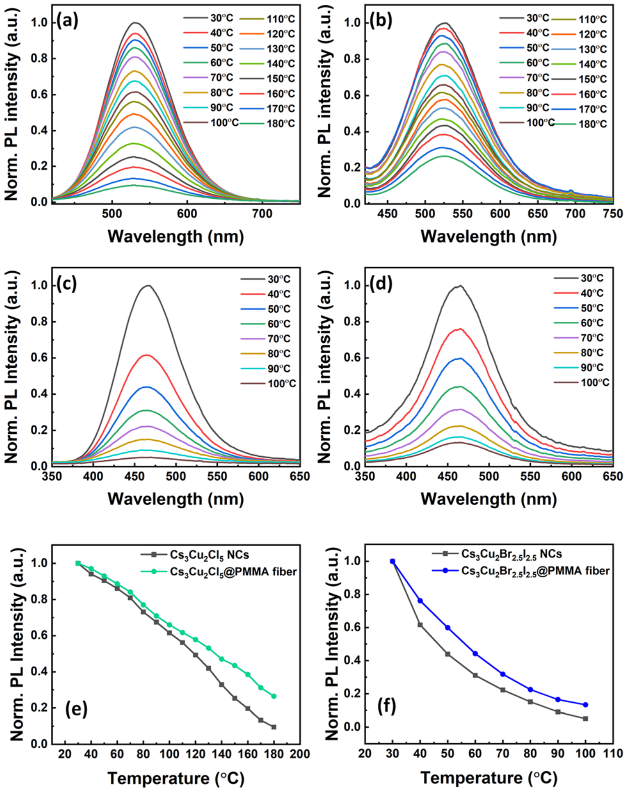

Fig. 7 Heat stability test: change in PL intensity of (a) $Cs_3Cu_2Cl_5$ NCs and (b) $Cs_3Cu_2Cl_5$@PMMA fiber films heated at temperatures ranging from 30 to 180 °C as shown in a legend. PL spectra of (c) $Cs_3Cu_2Br_{2.5}I_{2.5}$ NCs and (d) $Cs_3Cu_2Br_{2.5}I_{2.5}$@PMMA fiber films heated in a temperature range from 30 to 100 °C. (e) The relative change in PL intensities of $Cs_3Cu_2Cl_5$ NCs and $Cs_3Cu_2Cl_5$@PMMA fibers at different temperatures as represented in a legend. (f) The relative change in PL intensities of $Cs_3Cu_2Br_{2.5}I_{2.5}$ NCs and $Cs_3Cu_2Br_{2.5}I_{2.5}$@PMMA fibers at different temperatures as shown in a legend.

compared to their corresponding NC film counterparts. The $Cs_3Cu_2Cl_5$@PMMA fiber film retains 30% of the initial PL intensity at 180 °C, as can be seen from Fig. 7b, whereas the PL intensity for the bare $Cs_3Cu_2Cl_5$ NC film totally quenches. For the $Cs_3Cu_2Br_{2.5}I_{2.5}$@PMMA fiber film (see Fig. 7d), the PL retention is 22% of initial PL intensity at 80 °C compared to the $Cs_3Cu_2Br_{2.5}I_{2.5}$ NC film that retained 15% of its initial PL intensity. We also tested the heat stability of NCs and fiber films while placed on a hot plate and heated at a constant temperature. Further we fixed the temperatures for both NC films (80 °C for $Cs_3Cu_2Cl_5$ NCs and 60 °C for $Cs_3Cu_2Br_{2.5}I_{2.5}$ NCs) and observed the variation in PL over different time periods as shown in Fig. S6 (see ESI†). We chose a lower temperature for the $Cs_3Cu_2Br_{2.5}I_{2.5}$ NC film since these mixed halide NCs generally have lower stability compared to the $Cs_3Cu_2Cl_5$ NC film. The graphs reveal that the $Cs_3Cu_2Cl_5$@PMMA fiber film maintains 84% of the initial PL intensity compared to the bare $Cs_3Cu_2Cl_5$ NC film that quenched to 62% after 1 hour. Similarly, the $Cs_3Cu_2Br_{2.5}I_{2.5}$@PMMA fiber film retains 57% of the initial PL intensity compared to the $Cs_3Cu_2Br_{2.5}I_{2.5}$ NC film at 33% after the same time. In both cases, the fibers display better stability against heat treatment, which is beneficial for LED application. We further recorded the XRD and FESEM images of both NC and fiber films before and after thermal treatment to determine changes in structure (see Fig. S7, ESI†) and thin-film surface morphology (see Fig. S8, ESI†). A slight shift towards a lower angle in the XRD spectrum of the NCs is observed after thermal treatment. In addition to that, the FWHM of the XRD peaks also reduces which is due to agglomeration of the NCs among themselves and their fusion together. However, the morphology of the fiber films remained unchanged after thermal treatment. These results emphasize that the heat stability of the $Cs_3Cu_2Cl_5$ NCs is higher than that of mixed halide $Cs_3Cu_2Br_{2.5}I_{2.5}$ NCs. The heat stability of NCs can be further improved by embedding the NCs in polymer fibers which is due to the high heat absorption and release of these fibers.[63,72]

The flexibility of polymer fibers is an important property that can be exploited in the fabrication of efficient wearable display technologies. To test the flexibility of fibers, we coated the $Cs_3Cu_2Cl_5$@PMMA and $Cs_3Cu_2Br_{2.5}I_{2.5}$@PMMA fibers on PET substrates and studied their photophysical properties. The PL spectra of the fibers on PET substrates exhibit no significant variation in optical properties compared to the fibers coated on glass substrates, as presented in Fig. 8a and b. Insets of Fig. 8a and b show the photographic images of $Cs_3Cu_2Cl_5$@PMMA and $Cs_3Cu_2Br_{2.5}I_{2.5}$@PMMA fibers films bent under a UV lamp, showing bright green and blue PL emissions, respectively. The comparative PL intensity of NCs and their respective fiber films are shown in Fig. S9 (see ESI†). The PLQY values for $Cs_3Cu_2Cl_5$ and $Cs_3Cu_2Br_{2.5}I_{2.5}$ NCs films were calculated to be 55% and 26%, while those of $Cs_3Cu_2Cl_5$@PMMA and $Cs_3Cu_2Br_{2.5}I_{2.5}$@PMMA fiber films were measured as 47% and 19%, respectively. The morphology, shape, and surface coverage of the fibers are also unaffected, as observed in the FESEM images (see Fig. 8c and d). To check the flexibility of the NCs and fiber films on the

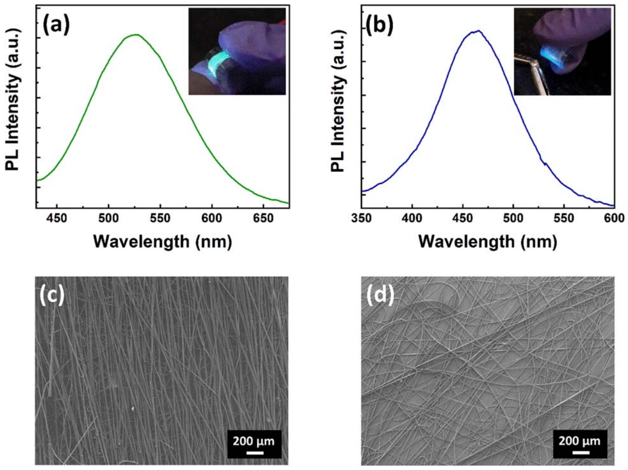

Fig. 8 PL spectra of (a) $Cs_3Cu_2Cl_5$@PMMA fibers and (b) $Cs_3Cu_2Br_{2.5}I_{2.5}$@PMMA fibers coated on PET substrates. Insets of (a) and (b) show photographic images of fibers coated on PET substrates and placed under a UV lamp. LR-FESEM images of (c) $Cs_3Cu_2Cl_5$@PMMA fibers and (d) $Cs_3Cu_2Br_{2.5}I_{2.5}$@PMMA fibers coated on PET substrates.

© 2023 The Author(s). Published by the Royal Society of Chemistry

Open Access Article. Published on 10 October 2023. Downloaded on 10/10/2024 9:31:03 AM.
This article is licensed under a Creative Commons Attribution-NonCommercial 3.0 Unported Licence.

PET substrate, the FESEM images of such films were recorded after bending and twisting about 50 times and the corresponding images are shown in Fig. S10 and S11 (see ESI†). It can be observed that in the case of NC films, the NCs are removed/peeled off from the substrate upon external stress. It may be due to the faint interaction of the NCs with the PET substrate and their tendency to agglomerate among themselves. Contrary to that, the FESEM images of both fibers reveal no sign of peel-off or removal from the PET substrate. The fibers are intact and attached to the surface of the substrate even after bending and twisting. Furthermore, no signs of breakage or crack (either single or bunch) on fiber strand/s were observed. These results show that the morphology and optical properties of the fibers remain unaffected even after bending, twisting, or any other physical stress. The high flexibility and stability of the fibers to external stress encourage their potential use in flexible/wearable displays.

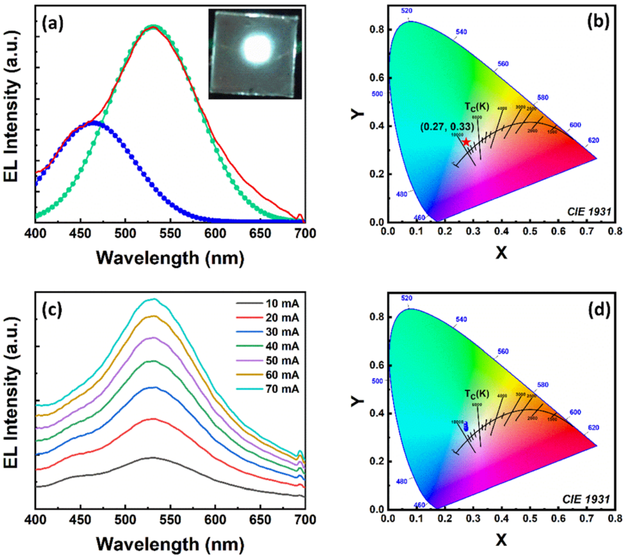

Fig. 9 (a) Deconvoluted EL spectrum of the color-converted WLED under driving current of 20 mA. Inset: photographic image of the glowing WLED. (b) Chromaticity coordinates (red star) of the fabricated WLED according to the 1931 CIE chromaticity diagram. (c) EL spectra of the WLED operated at different driving currents. (d) The corresponding color coordinates (blue dots) and CCT values of the WLED at different driving currents according to the 1931 CIE chromaticity diagram.

Finally, color-converting WLEDs were fabricated *via* coupling the green-emitting $Cs_3Cu_2Cl_5$ NC and blue-emitting $Cs_3Cu_2Br_{2.5}I_{2.5}$ NC films and placed over a 280 nm UV LED chip which was operated through an external source meter. At first we fabricated WLEDs from two separate films prepared from a mixture of blue and green colored NC solutions (NCs-LED) and with addition of PMMA into the same NC solution (NCs@PMMA-LED). The corresponding EL spectra and their CIE chromaticity diagram of these LEDs under a driving current of 20 mA are presented in Fig. S13 (in ESI†). In the case of the NCs-LED, the entire spectrum is dominated by the green emission having a broad peak at 512 nm (FWHM ∼ 132 nm) from $Cs_3Cu_2Cl_5$ NCs, and no contribution from $Cs_3Cu_2Br_{2.5}I_{2.5}$ NCs. The CIE color coordinate for the NCs-LED is obtained at (0.23, 0.25) with a CCT value of 10 629 K. In the case of the NCs@PMMA-LED, nearly a similar emission spectrum was obtained at 516 nm (FWHM ∼ 135 nm) with a CIE color coordinate of (0.27, 0.37) and a CCT value of 8475 K. Both the LEDs are not representing the pure white light emission since the contribution of blue emission is negligible. To tackle the issue we finally fabricated a color-converting WLED by coupling the $Cs_3Cu_2Cl_5$@PMMA fibers and $Cs_3Cu_2Br_{2.5}I_{2.5}$@PMMA fibers over the UV LED chip. The EL spectrum of the WLED under 20 mA driving current is shown in Fig. 9a. The photographic image of the WLED under operating conditions is shown in the inset of Fig. 9a. The deconvoluted EL spectrum reveals two emission peaks at 464 nm and 531 nm that originate from $Cs_3Cu_2Cl_5$@PMMA fibers and $Cs_3Cu_2Br_{2.5}I_{2.5}$@PMMA fibers, respectively. The combination of these two emissions results in a white-colored emission from the LED. The CIE chromaticity coordinates of the WLED were measured as (0.27, 0.33) at a 20 mA driving current, as presented in Fig. 9b, which is very close to the ideal white light source (0.33, 0.33).[88,89] The luminescence efficiency and CCT values were obtained as 69 Lm W^{-1} and 8703 K, respectively. Further, the bias current was varied in the range of 10–70 mA and the corresponding change in the EL spectra and CIE coordinates were recorded. The EL intensity increases gradually with an increase in applied current (see Fig. 9c). The CIE coordinates also shifted from (0.27, 0.33) at 10 mA to (0.27, 0.35) at 70 mA driving current and the CCT was changed from 8716 K (for 10 mA) to 8261 K (for 70 mA) as seen from Fig. 9d. The overall results are highly impressive and could be a first step towards the use of fiber composites in future flexible/wearable Pb-free LED fabrication.

4. Conclusion

In conclusion, green-emitting $Cs_3Cu_2Cl_5$ and blue-emitting $Cs_3Cu_2Br_{2.5}I_{2.5}$ NCs were synthesized by hot injection and LARP synthesis methods, respectively. The PLQY values of $Cs_3Cu_2Cl_5$ and $Cs_3Cu_2Br_{2.5}I_{2.5}$ NCs were around 65% and 32%, respectively. The XRD diffraction patterns of $Cs_3Cu_2Cl_5$ and $Cs_3Cu_2Br_{2.5}I_{2.5}$ NCs revealed highly crystalline orthorhombic perovskite phases. The as-synthesized NCs were monodisperse and had a uniform size distribution ranging from 4 to 5 nm. The composition of the NCs was confirmed by XPS and EDS measurements. To improve the NCs' stability, they were encapsulated in PMMA polymer fibers *via* an electrospinning process. The PLQY values for $Cs_3Cu_2Cl_5$ and $Cs_3Cu_2Br_{2.5}I_{2.5}$@PMMA fiber films resulted to be around 47% and 19%, respectively. The $Cs_3Cu_2Cl_5$ and $Cs_3Cu_2Br_{2.5}I_{2.5}$@PMMA fibers displayed better water stability than that of bare NCs due to the high hydrophobicity of PMMA fibers. The NC fibers coated on flexible PET substrates had enhanced surface coverage and showed high flexibility with no signs of breakage even after 50 cycles of bending and twisting. The fabricated WLED using $Cs_3Cu_2Cl_5$@PMMA and $Cs_3Cu_2Br_{2.5}I_{2.5}$@PMMA fiber films over a 280 nm UV LED chip showed white light emission under external bias with a luminous efficiency of 69 Lm W^{-1} and

© 2023 The Author(s). Published by the Royal Society of Chemistry

Open Access Article. Published on 10 October 2023. Downloaded on 10/10/2024 9:31:03 AM. This article is licensed under a Creative Commons Attribution-NonCommercial 3.0 Unported Licence.

a CCT value of 8703 K. The CIE chromaticity coordinates of the WLED is located at (0.27, 0.33), which is close to a white light emission. These findings reveal the potential of the electrospinning techniques to fabricate stable, efficient, and luminescent Pb-free perovskite fibers in future flexible/wearable display technologies.

Author contributions

S. B. and M. R. K. conceived the research idea and planned the experiments. M. R. K. and K. S. performed the synthesis, characterization, and related experiments. A. M. executed the FESEM imaging. The manuscript and revised version were written by S. B. and M. R. K. All authors have given approval to the final version of the manuscript. S. B. led the project.

Conflicts of interest

There are no conflicts to declare.

Acknowledgements

This research was supported by the Department of Science and Technology, India for financial support through the DST-INSPIRE Faculty research award (DST/INSPIRE/04/2017/000530). M. R. K., K. S., and A. M. acknowledge ICT-IOC Bhubaneswar for their fellowship support.

Notes and references

1 M. V. Kovalenko, L. Protesescu and M. I. Bodnarchuk, *Science*, 2017, **358**, 745–750.
2 Q. A. Akkerman, G. Rainò, M. V. Kovalenko and L. Manna, *Nat. Mater.*, 2018, **17**, 394–405.
3 A. Swarnkar, A. R. Marshall, E. M. Sanehira, B. D. Chernomordik, D. T. Moore, J. A. Christians, T. Chakrabarti and J. M. Luther, *Science*, 2016, **354**, 92–95.
4 Y. Zhao and K. Zhu, *Chem. Soc. Rev.*, 2016, **45**, 655–689.
5 X.-K. Liu, W. Xu, S. Bai, Y. Jin, J. Wang, R. H. Friend and F. Gao, *Nat. Mater.*, 2021, **20**, 10–21.
6 Y.-H. Kim, S. Kim, A. Kakekhani, J. Park, J. Park, Y.-H. Lee, H. Xu, S. Nagane, R. B. Wexler and D.-H. Kim, *Nat. Photonics*, 2021, **15**, 148–155.
7 W. Chen, S. Bhaumik, S. A. Veldhuis, G. Xing, Q. Xu, M. Grätzel, S. Mhaisalkar, N. Mathews and T. C. Sum, *Nat. Commun.*, 2017, **8**, 15198.
8 A. Dutta, R. K. Behera, P. Pal, S. Baitalik and N. Pradhan, *Angew. Chem., Int. Ed.*, 2019, **58**, 5552–5556.
9 Z. Wei, A. Perumal, R. Su, S. Sushant, J. Xing, Q. Zhang, S. T. Tan, H. V. Demir and Q. Xiong, *Nanoscale*, 2016, **8**, 18021–18026.
10 L. Lu, M. Sun, T. Wu, Q. Lu, B. Chen and B. Huang, *Nanoscale Adv.*, 2022, **4**, 680–696.
11 R. Chen, Y. Xu, S. Wang, C. Xia, Y. Liu, B. Yu, T. Xuan and H. Li, *J. Alloys Compd.*, 2021, **866**, 158969.
12 F. Gao, W. Yang, X. Liu, Y. Li, W. Liu, H. Xu and Y. Liu, *Chem. Eng. J.*, 2021, **407**, 128001.
13 V. Naresh, B. H. Kim and N. Lee, *Nano Res.*, 2021, **14**, 1187–1194.
14 A. Mohapatra, M. R. Kar and S. Bhaumik, *J. Alloys Compd.*, 2022, **927**, 166972.
15 A. Mohapatra, M. R. Kar and S. Bhaumik, *Front. Electron. Mater.*, 2022, **2**, 9.
16 X. Du, G. Wu, J. Cheng, H. Dang, K. Ma, Y.-W. Zhang, P.-F. Tan and S. Chen, *RSC Adv.*, 2017, **7**, 10391–10396.
17 S. Bhaumik, S. Ray and S. K. Batabyal, *Mater. Today Chem.*, 2020, **18**, 100363.
18 Z. Tan, J. Li, C. Zhang, Z. Li, Q. Hu, Z. Xiao, T. Kamiya, H. Hosono, G. Niu and E. Lifshitz, *Adv. Funct. Mater.*, 2018, **28**, 1801131.
19 P. Cheng, T. Wu, J. Zhang, Y. Li, J. Liu, L. Jiang, X. Mao, R.-F. Lu, W.-Q. Deng and K. Han, *J. Phys. Chem. Lett.*, 2017, **8**, 4402–4406.
20 M. R. Kar, M. R. Sahoo, S. K. Nayak and S. Bhaumik, *Mater. Today Chem.*, 2021, **20**, 100449.
21 C. Zhao, Y. Gao, D. Zhou, F. Zhu, J. Chen and J. Qiu, *J. Alloys Compd.*, 2023, **944**, 169134.
22 F. Zhang, X. Ji, W. Liang, Y. Li, Z. Ma, M. Wang, Y. Wang, D. Wu, X. Chen and D. Yang, *Mater. Horiz.*, 2021, **8**, 3432–3442.
23 J. Zhang, Y. Yang, H. Deng, U. Farooq, X. Yang, J. Khan, J. Tang and H. Song, *ACS Nano*, 2017, **11**, 9294–9302.
24 B. Yang, J. Chen, S. Yang, F. Hong, L. Sun, P. Han, T. Pullerits, W. Deng and K. Han, *Angew. Chem.*, 2018, **130**, 5457–5461.
25 X. Wang, Q. Shen, Y. Chen, N. Ali, Z. Ren, G. Bi and H. Wu, *J. Alloys Compd.*, 2022, **895**, 162610.
26 Z. Zhang, R. Zhao, S. Teng, K. Huang, L. Zhang, D. Wang, W. Yang, R. Xie and N. Pradhan, *Small*, 2020, **16**, 2004272.
27 W. Ke and M. G. Kanatzidis, *Nat. Commun.*, 2019, **10**, 965.
28 R. F. Ali, I. Andreu and B. D. Gates, *Nanoscale Adv.*, 2019, **1**, 4442–4449.
29 E. W.-G. Diau, E. Jokar and M. Rameez, *ACS Energy Lett.*, 2019, **4**, 1930–1937.
30 T. Krishnamoorthy, H. Ding, C. Yan, W. L. Leong, T. Baikie, Z. Zhang, M. Sherburne, S. Li, M. Asta and N. Mathews, *J. Mater. Chem. A*, 2015, **3**, 23829–23832.
31 N. Giesbrecht, A. Weis and T. Bein, *J. Phys.: Energy*, 2020, **2**, 024007.
32 N. K. Tailor, P. Maity, M. I. Saidaminov, N. Pradhan and S. Satapathi, *J. Phys. Chem. Lett.*, 2021, **12**, 2286–2292.
33 L. Zhou, Y. F. Xu, B. X. Chen, D. B. Kuang and C. Y. Su, *Small*, 2018, **14**, 1703762.
34 B. Yang, F. Hong, J. Chen, Y. Tang, L. Yang, Y. Sang, X. Xia, J. Guo, H. He and S. Yang, *Angew. Chem.*, 2019, **131**, 2300–2305.
35 F. Locardi, M. Cirignano, D. Baranov, Z. Dang, M. Prato, F. Drago, M. Ferretti, V. Pinchetti, M. Fanciulli and S. Brovelli, *J. Am. Chem. Soc.*, 2018, **140**, 12989–12995.
36 Z. Luo, Q. Li, L. Zhang, X. Wu, L. Tan, C. Zou, Y. Liu and Z. Quan, *Small*, 2020, **16**, 1905226.
37 R. Lin, Q. Guo, Q. Zhu, Y. Zhu, W. Zheng and F. Huang, *Adv. Mater.*, 2019, **31**, 1905079.

© 2023 The Author(s). Published by the Royal Society of Chemistry

Open Access Article. Published on 10 October 2023. Downloaded on 10/10/2024 9:31:03 AM.
This article is licensed under a Creative Commons Attribution-NonCommercial 3.0 Unported Licence.

38 T. Jun, K. Sim, S. Iimura, M. Sasase, H. Kamioka, J. Kim and H. Hosono, *Adv. Mater.*, 2018, **30**, 1804547.

39 H. Lee, D. Lee, H. Jin, D. Baek, M. K. Kim, J. Cha, S.-K. Kim and M. Kim, *Nanoscale Adv.*, 2022, **4**, 5189.

40 S. Zhao, C. Chen, W. Cai, R. Li, H. Li, S. Jiang, M. Liu and Z. Zang, *Adv. Opt. Mater.*, 2021, **9**, 2100307.

41 Y. Li, P. Vashishtha, Z. Zhou, Z. Li, S. B. Shivarudraiah, C. Ma, J. Liu, K. S. Wong, H. Su and J. E. Halpert, *Chem. Mater.*, 2020, **32**, 5515–5524.

42 X. Hu, Y. Li, Y. Wu, W. Chen, H. Zeng and X. Li, *Mater. Chem. Front.*, 2021, **5**, 6152–6159.

43 J. De Roo, M. Ibáñez, P. Geiregat, G. Nedelcu, W. Walravens, J. Maes, J. C. Martins, I. Van Driessche, M. V. Kovalenko and Z. Hens, *ACS Nano*, 2016, **10**, 2071–2081.

44 Z. Liu, Y. Bekenstein, X. Ye, S. C. Nguyen, J. Swabeck, D. Zhang, S.-T. Lee, P. Yang, W. Ma and A. P. Alivisatos, *J. Am. Chem. Soc.*, 2017, **139**, 5309–5312.

45 M. R. Kar, S. Ray, B. K. Patra and S. Bhaumik, *Mater. Today Chem.*, 2021, **20**, 100424.

46 Z. Liu, F. Li, G. Huang, F. Zhao, W. Zhang, G. Jiang, S. Cheng, Z. Fang, Q. Zhu and Y. Huang, *J. Alloys Compd.*, 2021, **888**, 161505.

47 S. Bhaumik, S. A. Veldhuis, Y. F. Ng, M. Li, S. K. Muduli, T. C. Sum, B. Damodaran, S. Mhaisalkar and N. Mathews, *Chem. Commun.*, 2016, **52**, 7118–7121.

48 G. H. Ahmed, J. Yin, O. M. Bakr and O. F. Mohammed, *ACS Energy Lett.*, 2021, **6**, 1340–1357.

49 X. Liu, W. Chen, J. Yang, X. Liang, X. Fang and W. Xiang, *ACS Appl. Electron. Mater.*, 2023, **5**, 2309–2317.

50 M. R. Kar, R. Chakraborty, U. Patel, R. Chakraborty, S. Ray, T. K. Acharya, C. Goswami and S. Bhaumik, *Mater. Today Chem.*, 2022, **23**, 100753.

51 S. Ray, A. Mohapatra and S. Bhaumik, *Mater. Adv.*, 2022, **3**, 4684–4692.

52 F. Zhang, Z.-F. Shi, Z.-Z. Ma, Y. Li, S. Li, D. Wu, T.-T. Xu, X.-J. Li, C.-X. Shan and G.-T. Du, *Nanoscale*, 2018, **10**, 20131–20139.

53 M. R. Kar, S. Kumar, T. K. Acharya, C. Goswami and S. Bhaumik, *RSC Adv.*, 2023, **13**, 5946–5956.

54 A. Mohapatra, S. Kumar, T. K. Acharya, C. Goswami and S. Bhaumik, *J. Alloys Compd.*, 2023, **947**, 169453.

55 Y. Wang, L. Varadi, A. Trinchi, J. Shen, Y. Zhu, G. Wei and C. Li, *Small*, 2018, **14**, 1803156.

56 J. Chen, X. Huang, Z. Xu and Y. Chi, *ACS Appl. Mater. Interfaces*, 2022, **14**, 33703–33711.

57 S. Vedi, T. Dheivasigamani, G. S. Selvam, T. Kawakami, N. Rajeswaran, S. Rajendran, A. Muthukaruppan, S. AlFaify and M. Shkir, *Biomater. Sci.*, 2022, **10**, 5956–5967.

58 V. Santhana, D. C. Greenidge, D. Thangaraju, R. Marnadu, T. Alshahrani and M. Shkir, *Mater. Lett.*, 2020, **280**, 128562.

59 J. Shi, W. Ge, W. Gao, M. Xu, J. Zhu and Y. Li, *Adv. Opt. Mater.*, 2020, **8**, 1901516.

60 S. Y. Lee, S. Jeon, J. Ahn, J. Bang, H. K. Woo, K.-j. Lee, B. K. Jung, T. Park, D. Son, J.-P. Ahn and S. J. Oh, *Appl. Surf. Sci.*, 2021, **563**, 150229.

61 A. Luzio, E. V. Canesi, C. Bertarelli and M. Caironi, *Materials*, 2014, **7**, 906–947.

62 X. Hu, Y. Xu, J. Wang, J. Ma, L. Wang and W. Jiang, *Adv. Fiber Mater.*, 2023, **5**, 183–197.

63 H. Liao, S. Guo, S. Cao, L. Wang, F. Gao, Z. Yang, J. Zheng and W. Yang, *Adv. Opt. Mater.*, 2018, **6**, 1800346.

64 Y. Sun, S. Cheng, W. Lu, Y. Wang, P. Zhang and Q. Yao, *RSC Adv.*, 2019, **9**, 25712–25729.

65 E. Ercan, P.-C. Tsai, J.-Y. Chen, J.-Y. Lam, L.-C. Hsu, C.-C. Chueh and W.-C. Chen, *ACS Appl. Mater. Interfaces*, 2019, **11**, 23605–23615.

66 P. C. Tsai, J. Y. Chen, E. Ercan, C. C. Chueh, S. H. Tung and W. C. Chen, *Small*, 2018, **14**, 1704379.

67 K. Lê, F. von Toperczer, F. Ünlü, G. Paramasivam, F. Mathies, E. Nandayapa, E. J. W. List-Kratochvil, T. Fischer, K. Lindfors and S. Mathur, *Adv. Eng. Mater.*, 2023, 2201651.

68 C. C. Lin, D.-H. Jiang, C.-C. Kuo, C.-J. Cho, Y.-H. Tsai, T. Satoh and C. Su, *ACS Appl. Mater. Interfaces*, 2018, **10**, 2210–2215.

69 W. Liu, H. Fu, H. Liao, Z. Liang, Y. Ye, J. Zheng and W. Yang, *J. Mater. Chem. C*, 2020, **8**, 13972–13975.

70 S. S. H. Abir, S. K. Gupta, A. Ibrahim, B. B. Srivastava and K. Lozano, *Mater. Adv.*, 2021, **2**, 2700–2710.

71 L.-C. Chen, C.-H. Tien, Z.-L. Tseng, Y.-S. Dong and S. Yang, *Materials*, 2019, **12**, 985.

72 D.-H. Jiang, Y.-H. Tsai, L. Veeramuthu, F.-C. Liang, L.-C. Chen, C. C. Lin, T. Satoh, S.-H. Tung and C.-C. Kuo, *APL Mater.*, 2019, **7**, 111105.

73 L. Xie, B. Chen, F. Zhang, Z. Zhao, X. Wang, L. Shi, Y. Liu, L. Huang, R. Liu, B. Zou and Y. Wang, *Photonics Res.*, 2020, **8**, 768–775.

74 B. M. Benin, D. N. Dirin, V. Morad, M. Wörle, S. Yakunin, G. Rainò, O. Nazarenko, M. Fischer, I. Infante and M. V. Kovalenko, *Angew. Chem., Int. Ed.*, 2018, **57**, 11329–11333.

75 T. Hu, M. D. Smith, E. R. Dohner, M.-J. Sher, X. Wu, M. T. Trinh, A. Fisher, J. Corbett, X. Y. Zhu and H. I. Karunadasa, *J. Phys. Chem. Lett.*, 2016, **7**, 2258–2263.

76 M. D. Smith and H. I. Karunadasa, *Acc. Chem. Res.*, 2018, **51**, 619–627.

77 R. Zhang, X. Mao, P. Cheng, Y. Yang, S. Yang, T. Wumaier, W. Deng and K. Han, *J. Energy Chem.*, 2019, **36**, 1–6.

78 S. Zhao, Q. Mo, W. Cai, H. Wang and Z. Zang, *Photonics Res.*, 2021, **9**, 187–192.

79 I. O. P. De Berti, M. V. Cagnoli, G. Pecchi, J. L. Alessandrini, S. J. Stewart, J. F. Bengoa and S. G. Marchetti, *Nanotechnology*, 2013, **24**, 175601.

80 D. H. Lee, R. A. Condrate and W. C. Lacourse, *J. Mater. NanoSci.*, 2000, **35**, 4961–4970.

81 L. M. Bronstein, X. Huang, J. Retrum, A. Schmucker, M. Pink, B. D. Stein and B. Dragnea, *Chem. Mater.*, 2007, **19**, 3624–3632.

82 T. Li, X. Mo, C. Peng, Q. Lu, C. Qi, X. Tao, Y. Ouyang and Y. Zhou, *Chem. Commun.*, 2019, **55**, 4554–4557.

83 H. Li, J. Jiao, D. Luo, D. Xiong and L. Gao, *Dalton Trans.*, 2022, **51**, 17883–17894.

84 D. Wilson and M. A. Langell, *Appl. Surf. Sci.*, 2014, **303**, 6–13.

85 J. Zhao, S. Cao, Z. Li and N. Ma, *Chem. Mater.*, 2018, **30**, 6737–6743.

© 2023 The Author(s). Published by the Royal Society of Chemistry

Open Access Article. Published on 10 October 2023. Downloaded on 10/10/2024 9:31:03 AM.
This article is licensed under a Creative Commons Attribution-NonCommercial 3.0 Unported Licence.

86 L. Li, Z. Jiang, M. Li, R. Li and T. Fang, *RSC Adv.*, 2014, **4**, 52973–52985.

87 A. J. Knight and L. M. Herz, *Energy Environ. Sci.*, 2020, **13**, 2024–2046.

88 C.-Y. Chang, A. N. Solodukhin, S.-Y. Liao, K. P. O. Mahesh, C.-L. Hsu, S. A. Ponomarenko, Y. N. Luponosov and Y.-C. Chao, *J. Mater. Chem. C*, 2019, **7**, 8634–8642.

89 X. Guo, G. D. Shen, B. L. Guan, X. L. Gu, D. Wu and Y. B. Li, *Appl. Phys. Lett.*, 2008, **92**, 013507.

© 2023 The Author(s). Published by the Royal Society of Chemistry